UDK 691.714:621.791
Original scientific article/Izvirni znanstveni članek

ISSN 1580-2949
Mater. Tehnol.

MICROSTRUCTURE AND FRACTURE MECHANISM OF WIRE ARC 316L STAINLESS STEEL WELDED JOINTS

MIKROSTRUKTURA IN MEHANIZMI LOMA ZVARNIH SPOJEV IZ NERJAVNEGA JEKLA 316L IZDELANIH S POSTOPKOM DODAJALNE TEHNOLOGIJE V OBLOKU ŽICE

Hang Dong, Yong Wang*, Zhiyuan Liu, Can Liu

School of Mechanical Science and Engineering, Northeast Petroleum University, 199 Fazhan Road, Daqing 163318, China

Prejem rokopisa – received: 2026-01-07; sprejem za objavo – accepted for publication: 2026-05-12

doi:10.17222/mit.2026.1640

This study investigates TIG-welded joints of wire arc additively manufactured 316L stainless steel. A pronounced <001> texture occurred in the fusion zone, with the strongest texture intensity observed in the columnar dendritic region, while the fusion zone center consisted of equiaxed grains with random orientations. The heat-affected zone exhibited a significant žthermo-mechanical' effect, with high-angle grain boundaries decreasing from 91 % to 56 %. Non-uniform microhardness was observed, with the minimum in the columnar dendritic zone. The joint achieved an ultimate tensile strength of 378.6 MPa. However, the dimples on the fracture surface were predominantly shallow and heterogeneously distributed, indicating constrained ductility despite the ductile fracture mode.

Keywords: WAAM, welding, mechanical properties, microstructure

V članku avtorji opisujejo raziskavo zvarnih spojev iz nerjavnega jekla 316L, ki so bili izdelani z dodajalno tehniko žično-obločnega varjenja TIG v zaščitni atmosferi in z volframovo elektrodo (angl.: Tungsten Inert Gas). Raziskava je pokazala, da se je v območju taljenja pojavila izrazita mikrostrukturna tekstura , pri čemer je bila najvišja intenzivnost teksture opažena v stebrastem dendritičnem območju, medtem ko je bilo središče območja taljenja sestavljeno iz enakoosnih kristalnih zrn z naključno orientacijo. V območju toplotno vplivane cone je bil viden pomemben »termo-mehanski« učinek, pri čemer se je delež velikokotnih kristalnih mej zmanjšal z 91 % na 56 %. Opažena je bila tudi neenakomerna mikrotrdota, z minimalnimi vrednostmi v stebrastem dendritičnem območju. Spoj je imel natezno trdnost 378,6 MPa. Vendar so bile jamice na površini loma pretežno plitve in heterogeno porazdeljene, kar kaže na omejeno duktilnost kljub duktilnemu (jamičastem) načinu loma.

Ključne besede: dodajalna tehnologija navarjenja, mehanske lastnosti, mikrostruktura

1 INTRODUCTION

WAAM employs an electric arc to melt and deposit 316L stainless steel (SS) wire layer by layer, subjecting the material to complex and repetitive thermal cycles.[1,2] This results in a non-equilibrium microstructure distinct from traditional wrought materials.[3] Consequently, WAAM-produced 316L SS exhibits unique and often anisotropic mechanical properties, such as direction-dependent deformation behaviour and orthotropic elastic characteristics.[4,5] When practical applications of WAAM components necessitate secondary TIG welding operations to create larger assemblies or integrate with existing structures, a critical and underexplored interface is formed between the distinct metallurgical characteristics of additively manufactured materials and conventional welding metallurgy.[2]

The high-heat-input characteristic of TIG welding can significantly alter a carefully solidified WAAM microstructure in the heat-affected zone (HAZ).[3] This may lead to grain coarsening, phase transformations, and changes in the distribution of secondary phases. For example, TIG welding of laser powder bed fusion 316L SS results in a fusion zone dominated by dendritic austenite and δ-ferrite, exhibiting a different hardness profile compared to laser-welded joints.[6] Recent studies have begun to investigate the influence of specific welding parameters on conventional 316L SS, demonstrating that shielding gas composition (e.g., additions of N_2 and He) and welding current significantly affect bead geometry, phase balance, and elemental distribution.[7,8] This underscores the necessity for a careful re-evaluation of welding procedures when the base material is a WAAM deposit with its own unique thermal history and mechanical characteristics.[5,9] Although the welding behavior of conventional wrought 316L SS has been extensively studied, the microstructural evolution and mechanical integrity of TIG-welded joints made entirely from WAAM-fabricated 316L SS remain underexplored.

Unlike wrought 316L, which possesses a fully recrystallized equiaxed grain structure and relatively homogeneous mechanical properties, WAAM 316L exhibits a strong <001> texture, cellular substructures, and a high proportion of high-angle grain boundaries

*Corresponding author's e-mail:
wangyongsll@163.com(Yong Wang)

© 2026 The Author(s). Except when otherwise noted, articles in this journal are published under the terms and conditions of the Creative Commons Attribution 4.0 International License (CC BY 4.0).

(HAGBs). These unique characteristics are expected to result in significantly different responses to subsequent TIG welding.[10] This study systematically investigates, for the first time, the coupled effect of WAAM-specific initial microstructure and TIG thermal cycles on the resulting heterogeneous microstructure, hardness distribution, and fracture behavior. Therefore, this study combines advanced microscopic characterization and mechanical testing to conduct a detailed analysis of the microstructure in the weld metal, HAZ, and WAAM base material, and assesses the mechanical behavior of the welded joint.

2 EXPERIMENTAL PRINCIPLES AND METHODS

The schematic diagrams of the WAAM and TIG welding processes are shown in **Figure 1**. Using a Yaskawa MA1440 six-axis robot equipped with an RD350 all-in-one inverter pulse gas shielded welding machine, 316L SS was additively manufactured under the protection of 99.99 % Ar. The additive current was set at 180 A, and the scanning speed was 1 mm/s. The WAAM 316L SS was then machined into thin plates with a thickness of 1.5 mm. The surfaces of the weldments were polished smooth and cleaned with organic solvents such as alcohol to remove oil and contaminants. A hair dryer was used to evaporate the alcohol, ensuring the weldments were clean and dry.

To prevent heat accumulation issues during the welding process, autogenous reciprocating TIG welding was performed on the two plates. The welding parameters were adjusted to a voltage of 12.8 V, a current of 70 A, and a wire feed speed of 2.5 mm/s. The flow rate of 99.99 % Ar was set at 15 L/min, resulting in a 316L SS welded joint. To meet the requirements for the subsequent microstructure analysis and performance testing, the welded joint was sectioned. Microstructural observation was conducted using an OLYMPUS-GX71 optical microscope. The cross-section of the specimen was scanned using an Oxford Symmetry S2 EBSD system with a scanning step size of 50 nm to obtain grain structure and orientation information.

Hardness testing of the welded joint was performed on an HVS-1000A hardness tester with a load of 300 gf and a dwell time of 15 s. Tensile testing was carried out on an AG-X DinoCapture2.0 Shimadzu testing machine at a loading speed of 0.5 mm/min. Fracture morphology was observed using a HITACHI S3400N scanning electron microscope (SEM).

3 RESULTS

Figure 2 shows the microstructure of the 316L SS welded joint. **Figure 2b** depicts the austenitic in the WAAM 316L SS base material (BM), characterized by a cellular substructure typical of additively manufactured materials.[11] **Figure 2c** shows the TIG welding heat-affected zone (HAZ). During the welding process, the HAZ experienced a rapid heating-and-cooling cycle. The temperature and duration were sufficient to initiate recrystallization but insufficient to allow complete grain growth, resulting in the formation of fine subgrain structures.[12] The blue line in **Figure 2a** represents the fusion

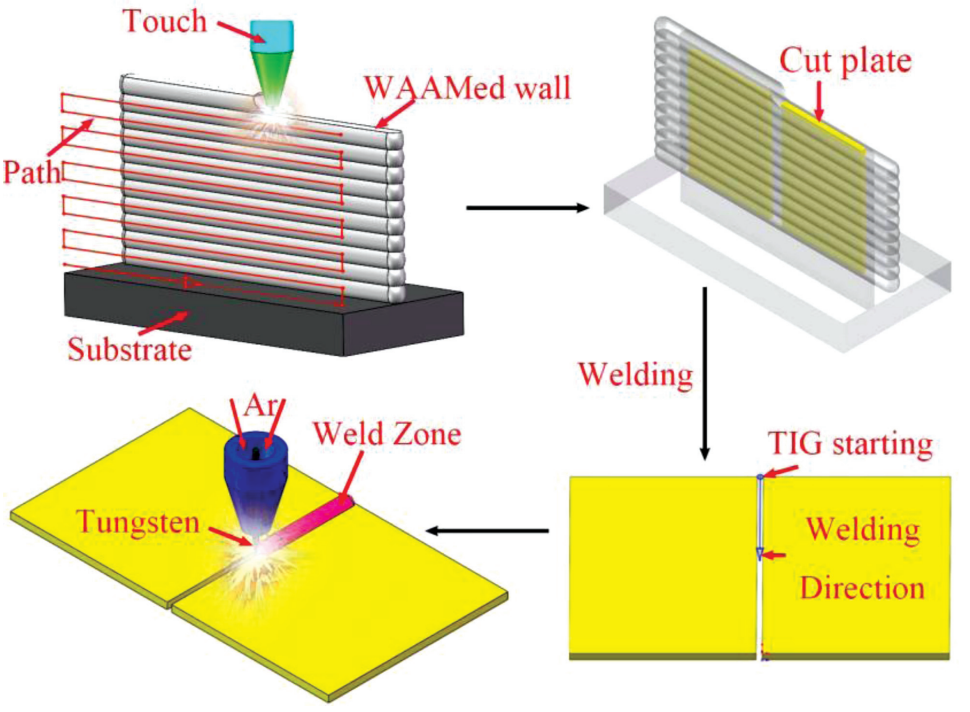

Figure 1: Schematic diagram of the process required for WAAMed 316L SS

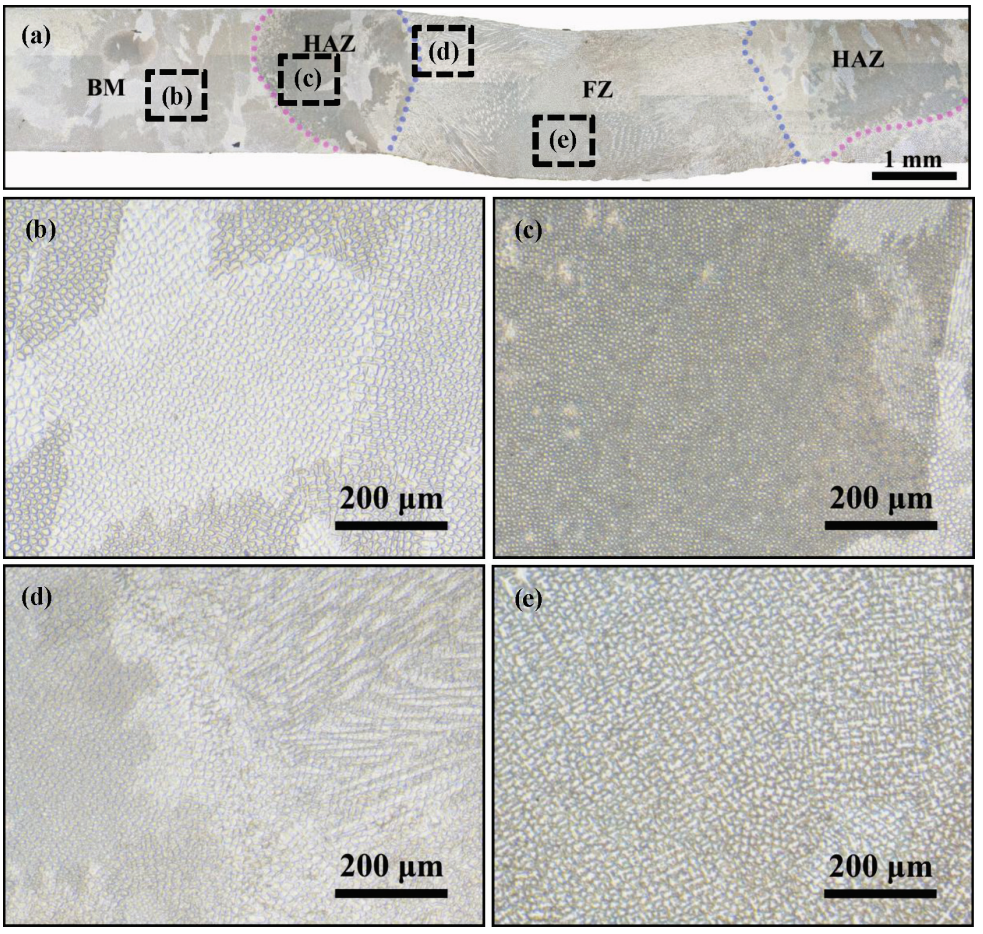

Figure 2: Microstructure of the WAAMed 316L SS joint: a) overview of the welded joint; b) BM showing cellular substructure; c) HAZ with fine subgrains; d) columnar dendritic zone near fusion line (FZ2); e) equiaxed grain zone at fusion zone center (FZ1)

line. The grain size in this region is generally larger than that in the BM. A layer of densely arranged columnar dendrites is present, with their growth direction approximately perpendicular to the fusion line. The difference in the temperature gradient at the liquid-solid interface during solidification between the weld center and the area near the HAZ caused the molten pool to solidify as columnar grains growing perpendicular to the fusion line.[13] **Figure 2e** presents the microstructure of the fusion zone (FZ). It illustrates that from the fusion line toward the FZ, the grain morphology transitions from columnar dendrites to equiaxed grains. Specifically, **Figure 2d** corresponds to the columnar dendritic region adjacent to the fusion line, while **Figure 2e** shows the equiaxed grain region at the weld center. This occurs because near the FZ, the temperature gradient is low, leading to a nearly uniform grain growth direction. In contrast, near the fusion line, the high temperature gradient promotes nucleation and growth of columnar dendrites.

Figure 3 presents the inverse pole figure (IPF) map of the welded joint, revealing a pronounced <001> texture within this region. The texture intensity is strongest in the columnar dendritic zone near the weld edge. This is because for face-centered cubic (FCC) metals, <001> is the preferred crystallographic orientation for growth. During the rapid solidification of the weld pool, the maximum temperature gradient is typically perpendicular to the fusion line, and crystals tend to grow along this temperature gradient direction, forming columnar grains. The welding thermal cycle induces recrystallization, during which grains preferentially reorient themselves along the low-energy <001> direction.[14] Concurrently, in the HAZ, the <001> orientation exhibits greater stability during the recovery stage due to the crystallographic anisotropy of dislocation rearrangement, leading to its selective retention.

In the FZ1 region (weld center, **Figure 2e**), the grain boundary misorientation map shows an irregular distribution of color blocks, with boundaries between blocks mostly corresponding to misorientation angles greater than 15°. This aligns with the grain boundary statistics indicating approximately 60 % HAGBs. This suggests that in the center of the molten pool, where the temperature gradient diminishes, a large number of nuclei form independently and grow randomly, ultimately resulting in an equiaxed grain structure with no strong preferred orientation.[15] For the BM region, the misorientation map shows a relatively random color distribution but contains

a network of blue lines. Combined with a high proportion of HAGBs (about 91 %), this indicates that the original WAAM microstructure is typical of a rapid solidification process. Although some substructure exists, it is primarily composed of HAGBs formed during solidification.

The local misorientation (KAM) maps presented in **Figures 3a2–d2** reveal distinct differences in strain distribution across the welded joint. In the HAZ (**Figure 3c2**), a significantly higher KAM signal is observed, particularly concentrated near grain boundaries and subgrain networks. This indicates localized plastic strain induced by welding thermal stress, consistent with the increased proportion of low-angle grain boundaries (44 %). In contrast, the columnar dendritic zone (FZ2, **Figure 3b2**) exhibits a uniformly low KAM value across the entire region, confirming near-complete strain elimination due to dynamic recovery. The BM (**Figure 3d2**) shows moderate and heterogeneously distributed KAM values, reflecting its original solidification-induced substructure without significant plastic deformation. The FZ1 (**Figure 3a2**) displays a low and homogeneous KAM distribution, consistent with equiaxed grain formation under low thermal gradient conditions.

The proportion of HAGBs in the BM is as high as about 91 %, which is consistent with the strong texture and abundant solidification grain boundaries formed during the WAAM process's rapid solidification.[16] In the HAZ, the proportion of HAGBs decreases to about 56 %, while the proportion of low-angle grain boundaries (LAGBs) increases significantly to about 44 %. This critical change indicates that the welding thermal cycle exerts a "thermo-mechanical" effect on the WAAM base material. On the one hand, the thermal cycle may cause some original HAGBs to disappear through migration or coalescence. On the other hand, plastic deformation induced by welding thermal stress introduces a high density of dislocations within the grains. These dislocations subsequently rearrange to form subgrain boundaries, i.e., LAGBs. In the weld metal regions (FZ1 and FZ2 from **Figures 2d, 2e**), the proportion of HAGBs recovers to about 60 %, entirely governed by the solidification process. The FZ2 columnar grain region exhibits distinct LAGB substructures within the grains. These substructures form due to the slight misorientations between dendrite arms during the directional growth of columnar grains. These substructures directly influence the path of dislocation movement, thereby affecting the work-hardening behavior in this region.

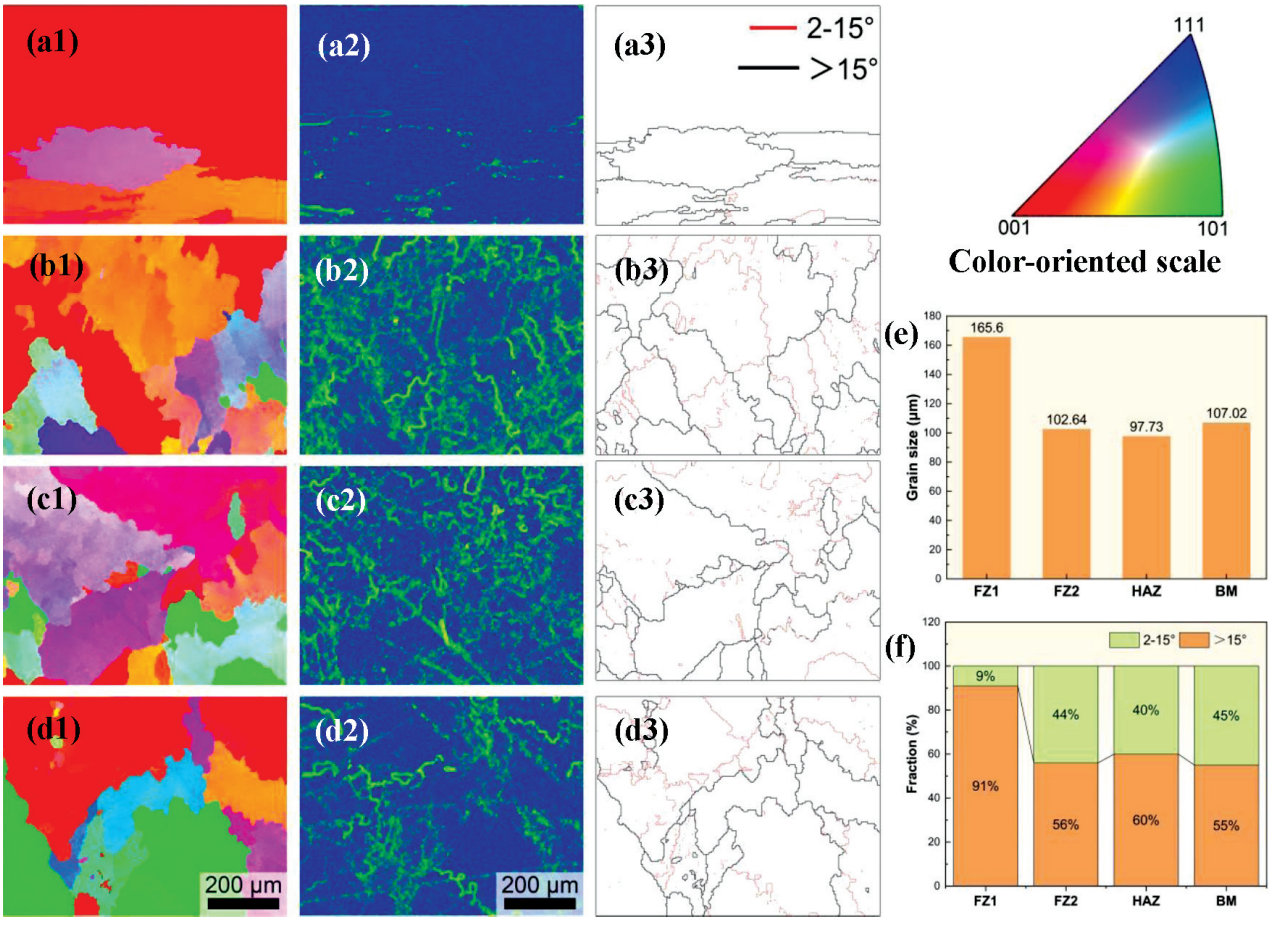

Figure 3: EBSD microstructure images of the 316L SS welded joints at different positions: a) FZ1, b) FZ2, c) HAZ, d) BM, (x1) IPF, (x2) local misorientation, (x3) distribution diagrams of HAGBs and LAGBs,(e) grain size statistics, f) statistical results of HAGB and LAGB

The microhardness distribution across the welded joint (**Figure 4a**) clearly reveals a non-uniform mechanical property gradient induced by the welding thermal process. The overall hardness fluctuates around 180 HV. A minimum hardness of 140.7 HV was measured in the columnar dendritic zone (FZ2) near the fusion line. This significant softening is attributed to three synergistic factors: (1) near-complete strain elimination as evidenced by the uniformly low KAM values in this region (**Figure 3b2**); (2) grain coarsening with an average grain size of approximately 18.5 μm, which is significantly larger than that of the BM (≈9.2 μm); and (3) the formation of a low-energy <001> texture that reduces dislocation density and resistance to indentation. In contrast, the fusion zone center (FZ1) composed of randomly oriented equiaxed grains exhibits a slightly higher hardness (≈165 HV) due to its moderate HAGB fraction (60 %) and absence of a strong texture. The HAZ shows intermediate hardness values (160–190 HV) attributable to partial recovery and the formation of subgrain boundaries (44 % LAGBs) that provide moderate strengthening. The BM exhibits the highest hardness (≈200 HV) due to its fine cellular substructure and high HAGB fraction (91 %).

The morphological characteristics of the gauge section of the 316 stainless steel (SS) tensile specimen after testing are shown in **Figure 4b**. Slip bands formed during plastic deformation are visible on the surfaces on both sides of the fracture. A distinct necking phenomenon is clearly observed at the fracture location. The tensile specimen surface was etched with hydrochloric acid-ferric chloride solution, and optical microscopy confirmed that the fracture occurred within the weld region. Dimensional measurements show that the weld length after stretching was 4.16 mm, compared to an original length of 3.44 mm, resulting in an elongation of 0.72 mm and an elongation rate of 20.9 % for the FZ. Combined with the microhardness analysis, the point of lowest hardness is located within the FZ. This localized softening is a typical manifestation of joint weakening, indicating insufficient strength in this region, which consequently acted as the weak link during tensile testing.

The fracture occurred consistently within the FZ, which can be directly correlated with the microhardness distribution. The FZ, particularly the columnar dendritic zone (FZ2), exhibited the lowest hardness (140.7 HV) and therefore acted as the mechanical weak link during tensile loading. The fracture mechanism is ductile, as evidenced by the presence of dimples and tear ridges in **Figure 4d**. However, a detailed examination reveals two distinct dimple morphologies: (i) fine, equiaxed dimples corresponding to the equiaxed grain zone (FZ1), indicating uniform plastic deformation; and (ii) coarse, shallow dimples associated with the columnar dendritic zone (FZ2), suggesting limited post-necking plasticity. The absence of large shear dimples or extensive microvoid coalescence bands further confirms constrained overall ductility (elongation of 23.99 %). This limited ductility is intrinsically linked to the microstructural heterogeneity: the softened, strain-free columnar zone localizes de-

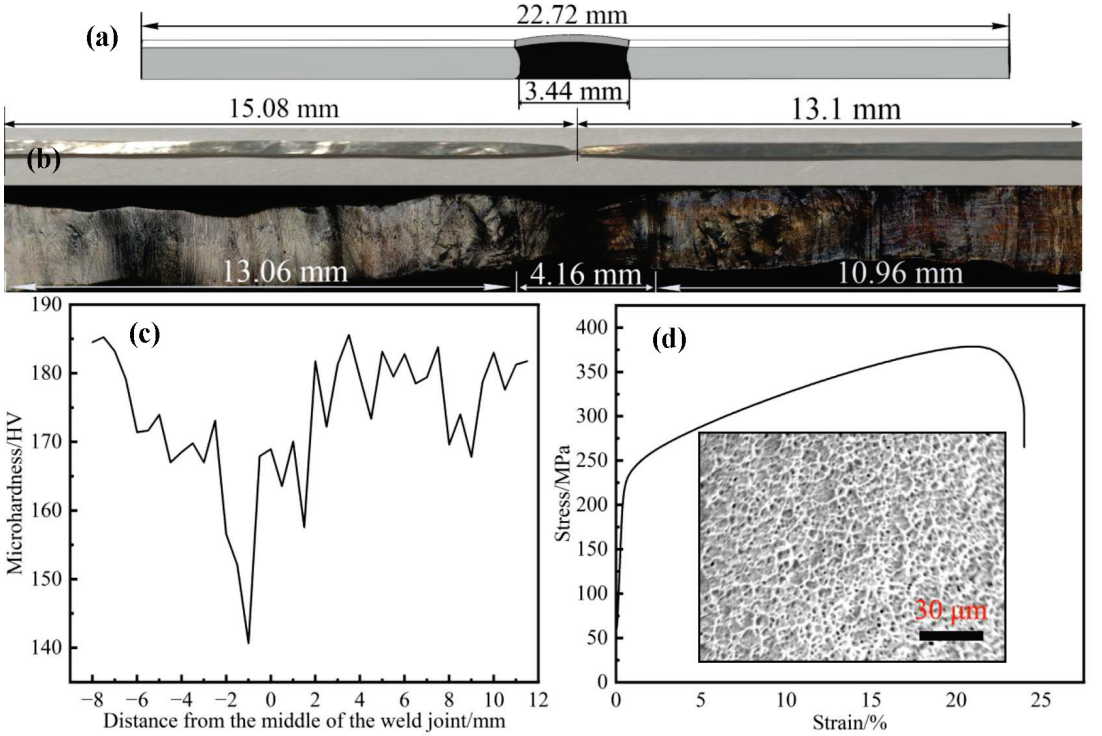

Figure 4: Mechanical properties of the WAAMed 316L SS weld joint: a) tensile sample size, b) fractured sample size, c) microhardness, d) stress-strain curve and fracture morphology

formation, while the surrounding harder regions restrict further plastic flow, leading to premature fracture after limited strain hardening.

4 CONCLUSIONS

(1) The welded joint of WAAMed 316L SS exhibits a gradient microstructure from the BM to the FZ, governed by the interaction between the initial WAAM <001> texture and the TIG thermal cycle. This interaction leads to a HAZ dominated by LAGBs (44 %) and a FZ that transitions from <001>-oriented columnar dendrites near the fusion line to randomly oriented equiaxed grains at the center.

(2) The minimum hardness is located in the columnar dendritic zone adjacent to the fusion line, resulting from three combined factors: strain elimination via dynamic recovery (evidenced by low KAM), grain coarsening (an average of ≈18.5 μm), and the formation of a low-energy <001> texture. The hardness reduction in this region is not merely a thermal effect but a consequence of the specific WAAM-origin microstructure.

(3) Fracture consistently initiates in the softened FZ, where the columnar dendritic zone acts as the mechanical weak link. The fracture surface reveals two distinct dimple populations, reflecting a heterogeneous microstructure. The constrained ductility (an elongation of 23.99 %) is intrinsically linked to the localized softening in the columnar zone, which limits strain redistribution and leads to premature failure after limited work hardening.

Declarations

The authors declare no conflict of interest.

Data availability

Data are available upon request.

Contributions

Conceptualization, methodology, writing, Hang Dong; formal analysis, Zhiyuan Liu; original draft preparation, Can Liu; review and editing, Yong Wang.

Funding and Acknowledgments

This work was supported by the Support Program of Heilongjiang Province for Basic Research of Outstanding Young Teachers (YQJH2025044), and the Selective Support Program of Heilongjiang Province for Returned Overseas Scholars.

5 REFERENCES

[1] J. Chen, C. Liu, K. Dong, S. Guan, Q. Wang, X. Zhang, Y. Peng, J. Kong, K. Wang, Crystallographic orientation dependence of dynamic deformation behaviours in additively manufactured stainless steel, J. Mater. Res. Technol., 24 (**2023**), 6699–6712, doi:10.1016/j.jmrt.2023.04.255

[2] K. Bin, P. Yao, P. Zhang, R. He, S. Zhong, Enhancing the strength and ductility of 316 L cladding via dual-pulse wire arc additive manufacturing process control, Mater. Today Commun., 41 (**2024**), 111108, doi:10.1016/j.mtcomm.2024.111108

[3] C. Wang, Y. H. Lu, P. Zhu, T. Shoji, In-situ observation of deformation behavior of the periodic structure in 316L stainless steel fabricated by wire and arc additive manufacturing, Mater. Charact., 203 (**2023**), 113162, doi:10.1016/j.matchar.2023.113162

[4] V. Ajay, J. Nakrani, N. K. Mishra, A. Shrivastava, Anisotropic fatigue crack propagation in wire arc additively manufactured 316L stainless steel, Int. J. Fatigue, 177 (**2023**), 107976, doi:10.1016/j.ijfatigue.2023.107976

[5] F. Le Bourdais, M. Mahmoudiniya, A. Gardahaut, L. A. I. Kestens, Resonant ultrasound elastic characterization of steel wire arc additive manufacturing samples, Mater. Charact., 220 (**2025**), 114603, doi:10.1016/j.matchar.2024.114603

[6] V. P. Dubey, M. Kopec, D. Przygucka, M. Pawlik, P. Wood, Z. L. Kowalewski, Effect of the printing orientation on the yield surface and its evolution reflecting plastic pre-deformation of additively manufactured stainless steel 316L, Int. J. Adv. Manuf. Technol., 140 (**2025**), 313–334, doi:10.1007/s00170-025-16296-y

[7] S. P. Subadra, E. Mayer, P. Wachtel, S. Sheikhi, Feasibility study on machine learning methods for prediction of process-related parameters during WAAM process using SS-316L filler material, Weld. World, 68 (**2024**), 3205–3214, doi:10.1007/s40194-024-01855-w

[8] P. Badoniya, M. Srivastava, P. K. Jain, A. Yadav, Investigation of bead morphology and mechanical behaviour for metal inert gas welding-based WAAM in pulsed mode metal transfer on 316LSi stainless steel, J. Adhes. Sci. Technol., 38 (**2024**) 5, 738–769, doi:10.2139/ssrn.4440909

[9] H. Qin, W. Zhu, H. Zhang, Effect of process parameters on bead geometry and microstructure of the stainless steel fabricated by wire arc additive manufacturing, J. Alloys Metall. Syst., 1 (**2026**), 100231, doi:10.1016/j.jalmes.2025.100231

[10] P. Wang, J. Zeng, D. Lu, W. Zheng, S. Zheng, B. Chen, Z. Gao, Nonlinear ultrasonic characterization of processing defects in wire arc additive manufacturing 316L stainless steel, Materials, 18 (**2025**) 4, 805, doi:10.3390/ma18040805

[11] C. Sasikumar, R. Oyyaravelu, Mechanical properties and microstructure of SS 316 L created by WAAM based on GMAW, Mater. Today Commun., 38 (**2024**), 107807, doi:10.1016/j.mtcomm.2023.107807

[12] P. S. Gowthaman, S. Jeyakumar, D. T. Sarathchandra, Study on Heat input effect of 316L stainless steel thin-walled parts processed by wire arc additive manufacturing, J. Mater. Eng. Perform., 34 (**2025**) 16, 17915–17932, doi:10.1007/s11665-024-10499-2

[13] Y. Di, Z. Zheng, S. Pang, J. Li, Y. Zhong, Dimension prediction and microstructure study of wire arc additive manufactured 316L stainless steel based on artificial neural network and finite element simulation, Micromachines, 15 (**2024**) 5, 615, doi:10.3390/mi15050615

[14] S. Thapliyal, P. Fernandez-Zelaia, Y. Lee, A. M. Rossy, L. Meyer, A. Nycz, Y. Yamamoto, M. M. Kirka, Considering interplay between multiple physical phenomena to elucidate single crystal-like texture, phase transformations, and mechanical behavior of directed energy deposited SS316L, Mater. Sci. Eng. A, 897 (**2024**), 146307, doi:10.1016/j.msea.2024.146307

[15] T. S. Nunes, T. G. de Sousa, D. B. Fernandes, L. O. Vilarinho, L. P. Brandao, Influence of current and CTWD on wire arc additive manufacturing 316L-Si stainless steel, Int. J. Adv. Manuf. Technol., 137 (**2025**), 4881–4896, doi:10.1007/s00170-025-15438-6

[16] S. H. Sun, K. Hagihara, T. Nakano, Effect of scanning strategy on texture formation in Ni-25 at.%Mo alloys fabricated by selective laser melting, Mater. Des., 140 (**2018**), 307–316, doi:10.1016/j.matdes.2017.11.060